Sintering of NaCl powder: Mechanisms and first stage kinetics

R. Goodall [*], J.-F. Despois, A. Mortensen

*Ecole Polytechnique Fédérale de Lausanne (EPFL), Laboratory for Mechanical Metallurgy, Institute of Materials,
CH-1015 Lausanne, Switzerland*

Abstract

Isothermal NaCl sintering experiments are conducted between 500 and 790 °C on powders 75, 100, 150 and 400 μm in average diameter. Along with literature data, the results are compared with theoretical predictions for the initial stage of sintering, to draw a general picture of the process over a wide spectrum of temperatures and particle sizes. Where densification is observed, the mechanism is grain boundary diffusion of material from boundary sources. As observed in previous work, there is a transition in dominance between this mechanism and the alternative, non-densifying, mechanism of evaporation–condensation. More detailed analysis shows that, after initial and effectively instantaneous plastic yielding driven by the surface energy, boundary diffusion will always dominate the initial stage of sintering for the conditions of this investigation, leading to some (possibly very small) degree of densification. For particles above about 150 μm at temperatures within 300 °C of the melting point of NaCl this mechanism will rapidly be displaced by evaporation–condensation, halting densification. An approximate equation is derived for the rate of sintering by evaporation–condensation in the presence of a finite-pressure inert atmosphere; the rate of this mechanism is found to be significantly reduced when sintering is carried out at pressures approaching atmospheric.
© 2006 Elsevier Ltd. All rights reserved.

Keywords: Sintering; Halides; NaCl

1. Introduction

Sodium chloride powders have long been used as a model system for the investigation of ceramic sintering behaviour; however, the system is also interesting from a practical point of view because sintered NaCl preforms are used in the manufacture of highly porous microcellular metals or ceramics by the replication process.[1]

Previous work on the sintering of NaCl, reviewed below, has provided a wide range of observations of powders of differing particle size exposed to a variety of sintering temperatures, but has left some questions that need to be resolved. It is the aim of this paper to bring a synthesis to earlier results, adding new experimental data where conditions have not been investigated, and to elucidate the behaviour of this compound throughout the sintering regime. The explanation of the different types of behaviour seen, and the global picture of the mechanisms operating at each stage will be provided using the same theoretical approach as for the production of sintering diagrams.

Sintering diagrams give information about the sintering behaviour of powdered materials. These were first introduced by Ashby,[2] and further developed by Swinkels and Ashby,[3] who included in their paper a map for the sintering of a pair of NaCl spheres. Such a plot displays graphically the rate-dominant sintering mechanisms that operate under different conditions of temperature, together with the density or the ratio of neck to particle radius for a given (uniform) initial particle size. The diagrams are formed using a series of equations that describe the rate of particle-particle neck growth as a function of the conditions, considering different mechanisms such as the six given in Fig. 1. By comparison of the rates predicted for each of these mechanisms in different regions of the diagram, fields of a given dominant mechanism may be identified. The plots can also contain information about the sintering rate and the stage of sintering reached, as fully explained in Refs. [2,3].

We restrict attention here to sintering in the absence of an applied pressure. The application of significant pressure will change the operating mechanisms, and different analysis applies.

---
* Corresponding author. Tel.: +41 21 693 4859; fax: +41 21 693 4664.
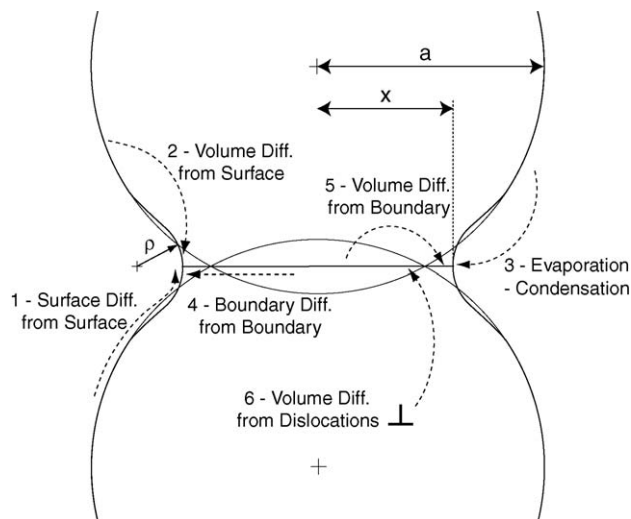*E-mail address:* russell.goodall@epfl.ch (R. Goodall).

Fig. 1. The six different sintering mechanisms considered by Ashby in the construction of sintering diagrams (after Ref. [2]).

Research in this area on NaCl suggests that plastic flow then becomes important.[4]

2. Pre-existing data for NaCl

Several previous workers have carried out sintering experiments on NaCl. Kingery and Berg[5] examined small chains of NaCl spheres of 61.5–70 μm diameter over the temperature range 700–750 °C. The rate of neck growth (measured optically) and the absence of densification of loose compacts led them to conclude that the operative mechanism was evaporation from the surface and condensation at the neck. Although not precisely stated, these experiments were probably performed under vacuum. A similar experiment was repeated under argon by Moser and Whitmore.[6] The absence of any centre-to-centre approach of the spheres led to the conclusion that the same mechanism was operating for spheres of average diameter in the range 98–227 μm between 730 and 795 °C.

Other workers did find densification during sintering; this cannot be a result of evaporation–condensation. Morgan et al.,[7] who worked with submicron ground (and therefore non-spherical) NaCl powder, found at 750 °C a volume reduction of up to 21.6%, which they attributed to plastic flow on the basis of a comparison with the behaviour of ThO₂.

Ammar and Budworth investigated whether different combinations of particle size and temperature produced densification.[8] For powder of a fixed mean diameter of 53 μm, densification was seen for temperatures in excess of 527 °C under both oxygen and nitrogen atmospheres. At a fixed temperature of 740 °C in oxygen, densification was seen for powders of mean particle diameter of 125 μm or less, but not for powders with 180 μm diameter or more. In later work the same authors noted that for an unspecified coarse powder the boundary for densification was in the 250–300 °C range.[9]

Several workers examined powders cold-pressed to differing degrees before sintering. Significant compression can complicate the situation by changing the curvature at the interparticle contact region and therefore the driving force for densification. Davidge examined 1 μm powder sintered in air, and found that densification occurred after 16 h at 550 °C, but not after a similar time at 400 °C.[10] After additional tests with applied pressure during the sintering process (i.e., in hot-pressing experiments), he concluded that the mechanism of densification under external pressure is plastic flow, in agreement with others,[4,11,12] changing to a diffusion mechanism when no pressure is applied. Tomlinson and Astle[13] investigated the sintering of pressed NaCl of various size ranges in air. They found no densification in the temperature range 650–750 °C for their size fraction 130–144 μm, though densification was found for all temperatures in the size range 44–50 μm. Powder of 2–3 μm diameter was used by Sata and Sakai,[14] who found densification throughout their tested temperature range of 500–700 °C, except under the conditions of high-pressure compaction prior to sintering (>60 MPa), where an expansion was seen. Further work suggested that this was due to the expansion of closed pores coupled with grain boundary relaxation after rapid grain growth.[15] This indicates that rate data may not be reliable where the powders are highly pressed before sintering.

Thompson and Munir[16] sieved a wide range of NaCl sizes, from <38 to 180 μm, but found that the mean particle size range was only 12–18 μm as a result of many smaller particles agglomerating on the surface of the larger ones retained by the sieves. These particles were pressed and then sintered in air at 700–775 °C, and in all cases some densification was observed. The amount of densification was seen to fall off as the nominal particle size increased, consistent with the idea of a limiting size; however, it must be borne in mind that densification in these blended powders will be dominated by the smaller NaCl grains, larger grains essentially serving as non-percolating inert inclusions that slow, but do not prevent, densification.[17] Indeed, percolation of the larger particles is not expected in these blends given that smaller particles dominate in number and are stuck to the surface of the larger particles.

All these results are plotted in Fig. 2 along with the experimental data obtained here, which we describe next.

3. Experimental

Much of the existing literature is focussed on the sintering behaviour in the temperature range 650–750 °C, as this is the range where sintering of NaCl would be most sensibly carried out. To explore the behaviour more widely, comparison was required with results from other particle sizes and shapes, and different temperatures.

The sintering of NaCl powder obtained by sieving of ground salt (CP1 grade, Salines de Bex, Bex, Switzerland) between 63 and 90 μm grade sieves (ISO 565) was monitored using a dilatometer. This powder had a mean particle size of 75 μm (Fig. 3a). Samples were cold isostatically pressed under relatively low pressure (10 MPa), to allow free-standing cylindrical specimens of 10 mm diameter and 15–20 mm height to be placed in the dilatometer. Free-standing specimens avoided the possibility of interactions with a support during sintering. The pre-pressing density was found to be 0.59 ± 0.01, which increased
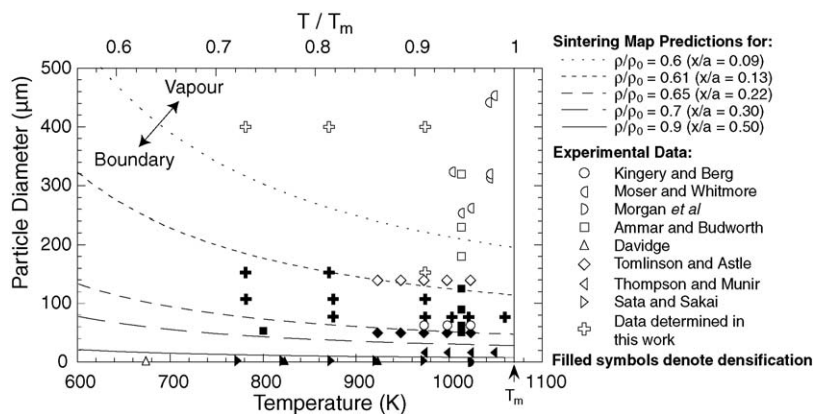
Fig. 2. Comparison of experimental data (from the literature and determined here) for the sintering behaviour of NaCl powders of differing particle sizes at different temperatures with the predicted regions of dominance of different mechanisms in vacuum, determined by the sintering diagram equations as a function of relative density. Filled-in symbols show where densification has been observed or reported; hollow symbols denote experiments where no noticeable densification was found. Experimental data are from this work and from Refs. [5–8,10,13,14,16].

to 0.63 ± 0.01 after the pressing step. The samples were then supported in the furnace of a dilatometer between a silica support and a silica push rod. The pressure imposed by the rod on the sample was evaluated to be 4 kPa and is neglected in the fol-

Fig. 3. SEM micrographs of NaCl crystals used in the experiments performed in this work: (a) as-sieved grains of 75 μm mean diameter and (b) 75 μm mean diameter spherical grains.

lowing analysis. The furnace was taken to the target temperature in air and allowed to stabilise, and then the displacement change measured by the push-rod was recorded for a period of at least 16 h. Temperatures of 586, 630, 670 and 701 °C were used (at higher temperatures deformation was found to be uneven and to give unreliable results). The change in linear dimension was measured throughout the sintering procedure. It was then corrected to account for the thermal expansion of the material, and used to calculate the change in the relative sample density during the experiment, assuming uniform dimensional changes.

Simpler experiments were additionally performed on powders of mean particle size 75, 100, 150 and 400 μm, examining the changes in dimensions of powder preforms sintered for at least 24 h in a graphite-coated alumina crucible at 500, 600 and 700 °C under flowing argon. Small quantities of the 75, 150 and 400 μm powders were also melted in the flame of a propane torch after preheating in air, and solidified in-flight in air (details of the process can be found in Ref. [18]). As seen in Fig. 3b, spherical powders were thus produced, allowing comparison with the sintering of the less regular angular particles (Fig. 3a). A small number of samples were also cold isostatically pressed at 5–10 MPa before sintering, and were mounted and polished after different sintering times to observe the change in structure.

4. Results and discussion

4.1. Experimental results

The observed densification or non-densification behaviours of all the sintering experiments performed here are indicated on Fig. 2. Examples of micrographs of polished 2D sections through the pressed and sintered compacts of both 75 μm NaCl (that did show densification) and 400 μm NaCl (that did not) are given in Figs. 4 and 5, respectively. With the former, the density increase is evident, as is the rounding of the pore surfaces. With the latter, the particles show some rounding; however, the density remains unaffected.

These results are consistent with the majority of the literature, although the results for powder of 75 μm mean diameter
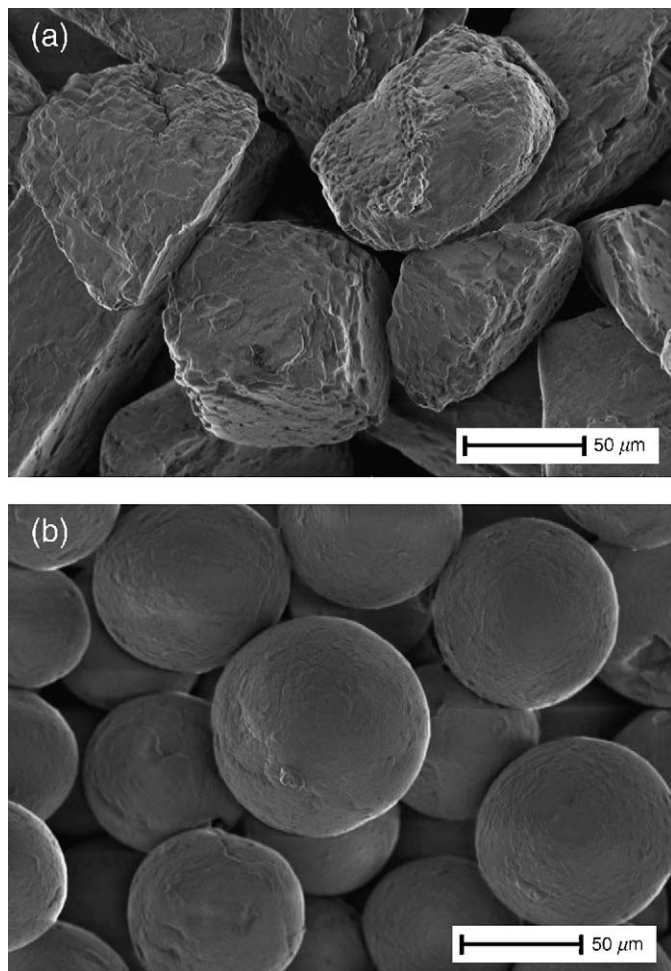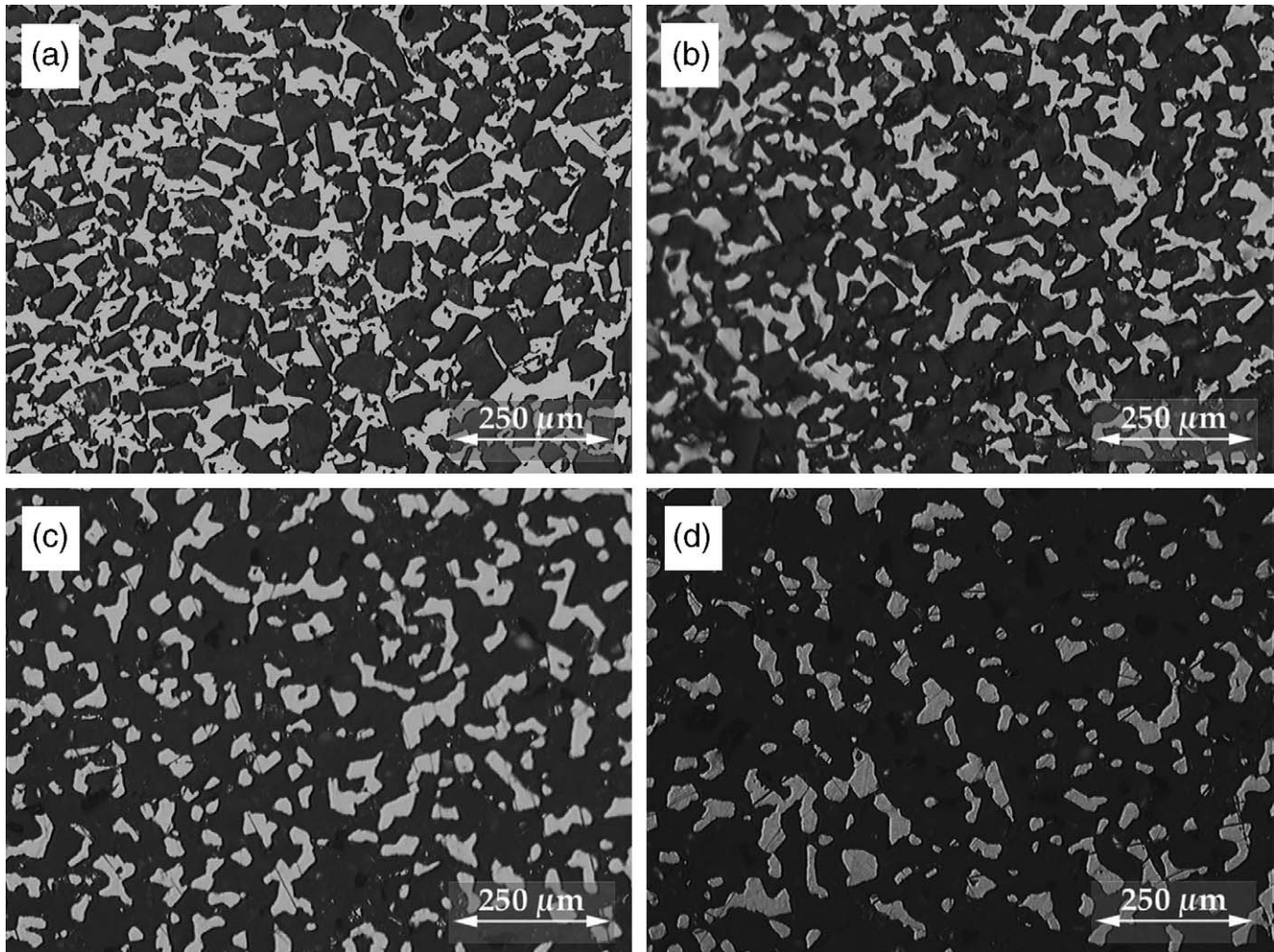
Fig. 4. Optical microscope images of polished 2D sections through NaCl preforms, initial powder 75 μm, cold isostatically pressed at 6 MPa, initial density 66% and sintered for (a) 0 h, (b) 2 h, (c) 9 h and (d) 25 h at 755 °C. Dark phase is NaCl, light phase is mounting resin.

show densification very close to the region on the map where Kingery and Berg did not find any.[5] The difference is likely to be due to the experimental conditions, as suggested by Ammar and Budworth.[8] Indeed, as will be shown below the presence of gas at one atmosphere pressure slows the evaporation–condensation process. Hence, this mechanism is slowed in the present experiments compared to those of Kingery and Berg, whose equipment featured a vacuum capability which was in all likelihood used.[6] It was also suggested by Ammar and Budworth that the friction between the spheres used in Kingery and Berg's experiment and the glass slide they were placed on may have reduced the centre-to-centre approach of the spheres.[8]

In all cases the same behaviour was observed with spherical powders as with the angular particles although, where densification occurred, there was often a greater total change in density measured after sintering with the angular particles. This suggests that, although the dominant mechanism is not affected on a large scale, sintering proceeds initially at a slightly higher rate for the angular particles. This is probably because the small, irregular initial contacts between rough particles at first sinter faster than the smooth contacts between spheres of similar volume.

The data gathered using the dilatometer allow an analysis of the process to be carried out. The sintering map discussed later suggests that, apart from some effectively instantaneous plastic yielding, time-dependent densification occurs under the conditions of all the experiments by grain boundary diffusion of material from the grain boundary across the neck between particles; Ashby gives the following equation for the rate of sintering by this mechanism[19]:

$$\frac{d\Delta}{dt} = \frac{129\delta_b D_b \gamma_s \Omega}{kTa^4} \frac{\Delta^2 (2\Delta - \Delta_0)}{\Delta - \Delta_0} \tag{1}$$

where a is the initial particle radius, Δ is the relative compact density at time t and Δ_0 is the initial relative compact density ($\Delta = \rho/\rho_0$ and $\Delta_0 = \rho_i/\rho_0$, where ρ is the powder compact density, ρ_i is the initial compact density and ρ_0 is the density of the non-porous material, all in kg m^{-3}). Δ_0 was taken equal to 0.63, the initial relative density of the cold-pressed powders (close to random dense sphere packing). Other terms are defined in Table 1, where their values are also given. Eq. (1) may be inte-
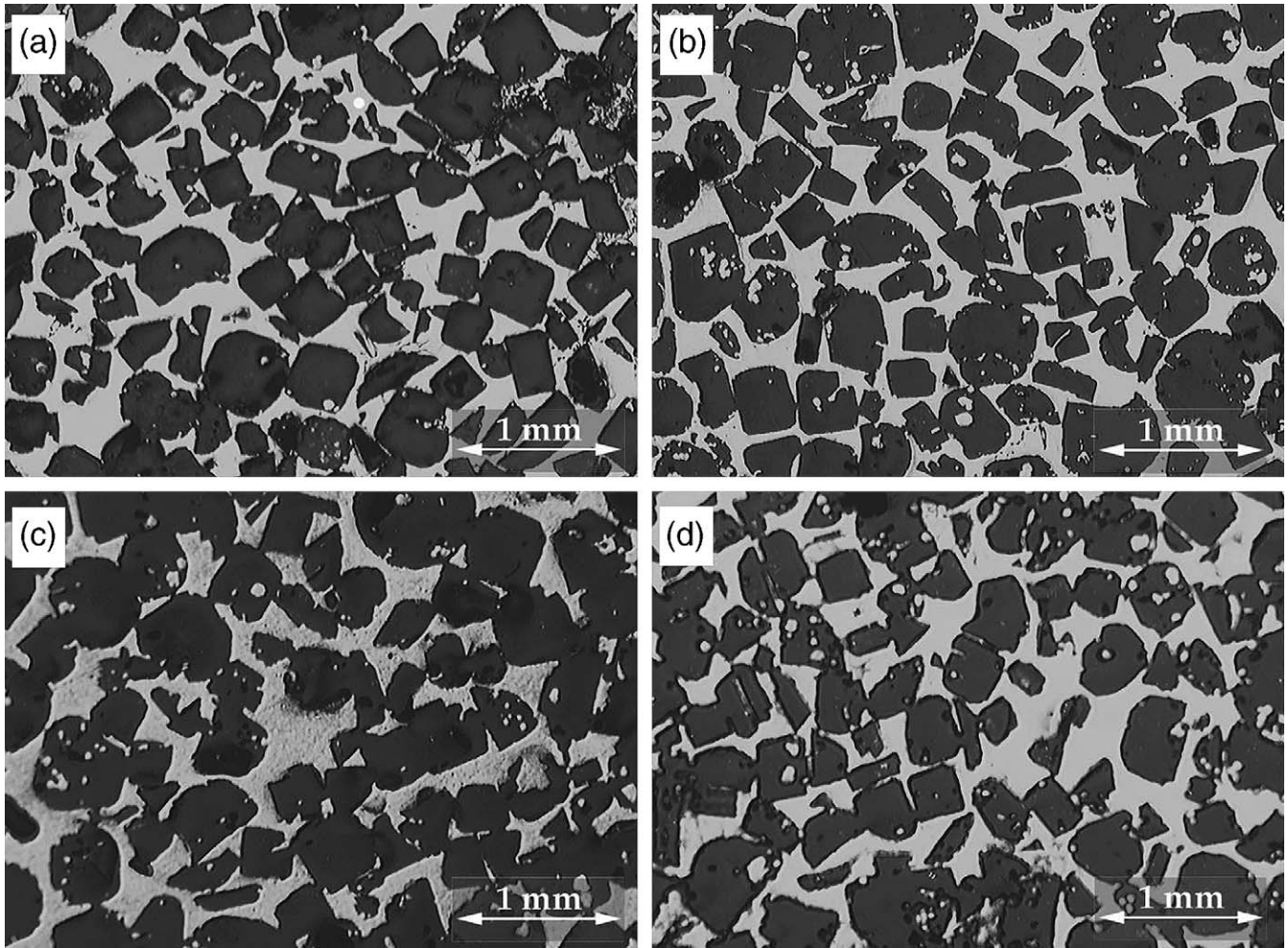
Fig. 5. Optical microscope images of polished 2D cuts of NaCl preforms, initial powder 400 μm, cold isostatically pressed at 10 MPa, initial density 72% and sintered for (a) 0 h, (b) 8 h, (c) 27 h and (d) 76 h at 755 °C. Dark phase is NaCl, light phase is mounting resin. Note that pores are visible within the NaCl particles; these correspond to pits emanating from the particle surfaces.[26]

grated to yield:

$$\frac{1}{\Delta_0} - \frac{1}{\Delta} + \frac{1}{\Delta_0}\ln\left(\frac{\Delta}{2\Delta - \Delta_0}\right) = \frac{129\delta_b D_b \gamma_s \Omega}{kTa^4}t. \qquad (2)$$

Therefore, plotting the left hand side of this equation against time should yield straight lines where sintering occurs by boundary diffusion. It is demonstrated in Fig. 6a that this is the case for the sintering data found using the dilatometer, indicating that this mechanism is indeed responsible for the densification observed in these experiments. Further analysis is possible, as the activation energy for grain boundary diffusion is contained in the term D_b. Taking the slope of each of the straight lines in Fig. 6a and plotting the natural logarithm of (slope × temperature) against $1/T$ should yield a straight line with slope -Q/R. This graph, shown in Fig. 6b, gives an activation energy of 150 kJ mol^{-1}, very close to the literature value of 155 kJ mol^{-1}.[20]

The data of Ammar and Budworth can be used as an additional check for slightly different conditions. Their data, Fig. 7a (replotted from Fig. 1 of Ref. [8]), are collapsed onto a single curve by the multiplication of the time by $\exp(-Q/RT)$ with $Q = 155$ kJ mol^{-1}, Fig. 7b. This once again confirms

that grain boundary diffusion is the operating densification mechanism.

4.2. Construction of the sintering diagram

Relevant equations and parameters allowing the derivation of sintering mechanism maps for NaCl are given by Ashby and co-workers.[2,3,20] Basic equations for the rate of neck growth driven by each of the six mechanisms depicted in Fig. 1 are given in Ref. [2]. In later work, Swinkels and Ashby introduced additional boundary conditions for the equations, describing the contributions of these different mechanisms. For example, the flux of material diffusing to the neck from grain boundary sources (Mechanism 4) is required to be in balance with the rate at which this material is distributed by surface diffusion, and the resulting change in the local neck curvature must be accounted for in the driving force.[3] While increasing the rigour of the equations, numerical methods become required for their solution. As the range of conditions considered here is wide, the precision of the earlier equations of Ref. [2], which give analytical solutions, is sufficient. Additional potential densification mechanisms are

Table 1
The properties of NaCl used in constructing the diagram

Property	Value	Ref.
Shear modulus at 300 K, G	1.51×10^{10} Pa	[20]
Temperature coefficient of G, t_G	-0.73	[20]
Yield stress at 300 K, σ_y	33 MPa	[27]
Tempeature coefficient of σ_y, t_{σ_y}	-0.95	[27]
Surface diffusion pre-exponential, D_{s0}	2.51×10^{-2} m^2 s^{-1}	[3]
Surface diffusion activation energy, Q_s	217 kJ mol^{-1}	[3]
Volume diffusion pre-exponential, D_{v0}	2.50×10^{-2} m^2 s^{-1}	[20]
Volume diffusion activation energy, Q_v	217 kJ mol^{-1}	[20]
Boundary diffusion pre-exponential, D_{b0}	7.77×10^{-1} m^2 s^{-1}	[20]
Boundary diffusion activation energy, Q_b	155 kJ mol^{-1}	[20]
Core diffusion pre-exponential, $a_c D_c$	4.9×10^{-19} m^4 s^{-1}	[20]
Core diffusion activation energy, Q_c	155 kJ mol^{-1}	[20]
Vaporisation pre-exponential, P_{v0}	2.97×10^{-10} Pa	[3]
Vaporisation activation energy, Q_v	182 kJ mol^{-1}	[3]
Dorn constant (power law creep), A	660	[20]
Power law creep exponent, n	3.6	[20]
Surface thickness (=Burgers vector), δ_s	3.99×10^{-10} m	[20]
Boundary thickness (=2 × Burgers vector), δ_b	7.98×10^{-10} m	[20]
Surface energy, γ_s	0.28 J m^{-2}	[3]
Atomic volume, Ω	4.49×10^{-29} m^3	[20]
Theoretical density, ρ_0	2170 kg m^{-3}	[28]
Dislocation density, N	10^{14} m^{-2}	[3]
Melting temperature, T_m	1070 K	[20]

(a)

(b)

Fig. 7. Sintering data for NaCl powder of mean diameter 53 μm under oxygen from Ammar and Budworth,[8] showing (a) their data, and (b) their data collapsed onto a single curve by multiplying the time by $\exp(-Q/RT)$, with $Q = 155$ kJ mol^{-1}, the activation energy for grain boundary diffusion in NaCl.

(a)

(b)
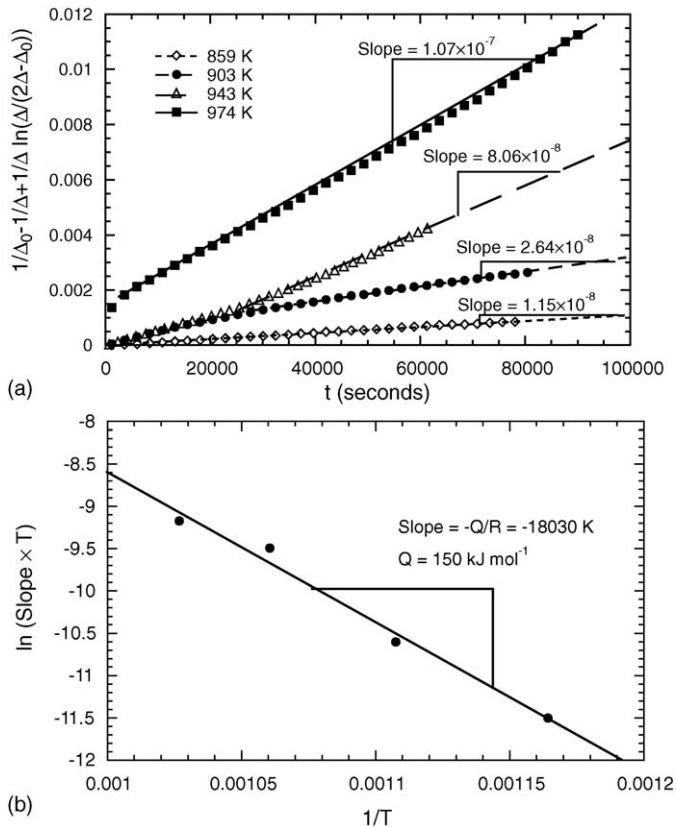
Fig. 6. Sintering data for 75 μm NaCl powder determined in this work, plotting (a) the Ashby Δ-based parameter for sintering controlled by grain boundary diffusion against time to produce straight lines, and (b) the natural logarithm of the straight line gradients multiplied by the temperature against the reciprocal temperature, allowing the activation energy to be estimated.
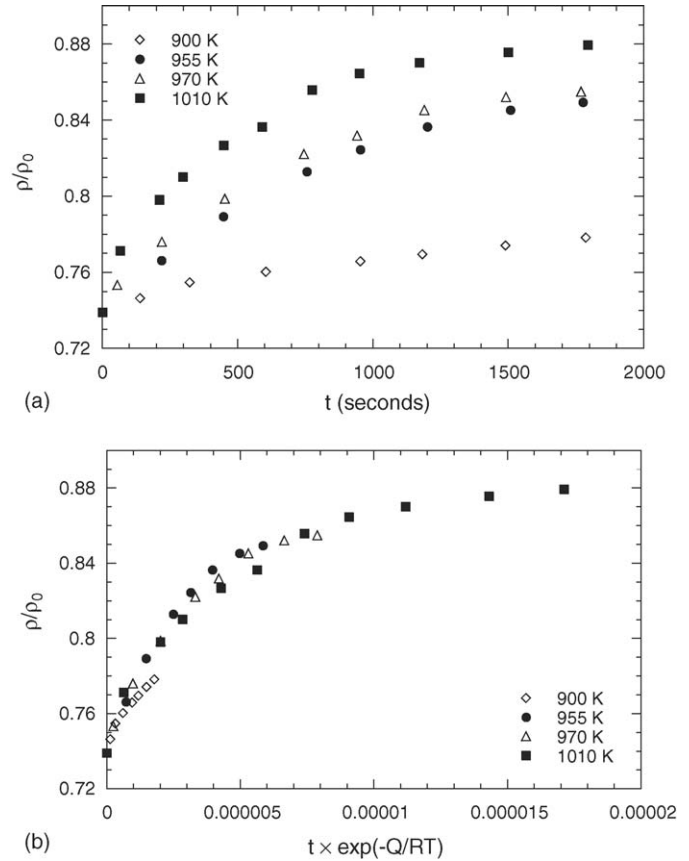
plastic flow of the powder particles, by power law creep or plastic yielding. Similar equations for the rate of neck growth also exist, as discussed in detail below.

We look only at Stage 1 behaviour. This corresponds to the stage at which the structure still consists of particles connected by necks, before the pores become spherical. We do so because, in all the experiments performed or reviewed here, it is the initial sintering behaviour that has been recorded, and also because only Stage 1 sintering is of interest for replication processing of microcellular materials. We also assume that the grain size in the powder is not significantly smaller than the particle diameter; this is simply because such is generally the case in ordinary salt powders. We focus for now on sintering in vacuum, and then relax this assumption in the last section.

For monosized spherical powder compacts, the relation between relative neck radius and compact density in Stage 1 sintering is:

$$\frac{x}{a} = \frac{1}{\sqrt{3}}\left[\frac{\Delta - \Delta_0}{1 - \Delta_0}\right]^{1/2} \tag{3}$$

where x is the neck radius, a is the particle radius, Δ the powder compact relative density and Δ_0 the initial relative density of the compact.[21] For random sphere packing Δ_0 is typically 0.54–0.64[3]; here, the mean loose powder packing value observed

with the angular salt powder, 0.59, has been used. The end of Stage 1 corresponds roughly to $\Delta = 0.9$; the maximum value that x/a can take during Stage 1 is thus around 0.5.

To determine the dominant mechanism, the following equations for the rate of each mechanism treated by Swinkels and Ashby (1–6 in Fig. 1) are evaluated and compared[2]:

$$\dot{x}_1 = 2D_s\delta_s FK_1^3 \tag{4}$$

$$\dot{x}_2 = 2D_v FK_1^2 \tag{5}$$

$$\dot{x}_3 = P_v F \left(\frac{\Omega}{2\pi\rho_0 kT}\right)^{1/2} K_1 \tag{6}$$

$$\dot{x}_4 = \frac{4D_b\delta_b FK_2^2}{x} \tag{7}$$

$$\dot{x}_5 = 4D_v FK_2^2 \tag{8}$$

$$\dot{x}_6 = \frac{4}{6}K_2 Nx^2 D_v F \left(K_2 - \frac{3Gx}{2\gamma_s a}\right) \tag{9}$$

where F (a group of parameters) and K_1 and K_2 (curvature differences driving some of the mechanisms) are given by:

$$F = \frac{\gamma_s \Omega}{kT} \tag{10}$$

$$K_1 = \left(\frac{2(a-x)}{x^2} - \frac{1}{x} + \frac{2}{a}\right)$$
$$\times \left(1 - \frac{x}{0.74a - ([\rho_0 - \rho_i]/3\rho_0)^{1/3}a}\right) \tag{11}$$

$$K_2 = \left(\frac{2(a-x)}{x^2} - \frac{1}{x}\right) \tag{12}$$

Remaining terms of these equations are defined in Table 1, which also gives the values used in the calculation.

These equations suggest[3] that for NaCl only two of these original six mechanisms will dominate within the ranges considered: (i) grain boundary diffusion from grain boundary sources (Mechanism 4), which will lead to densification, and (ii) evaporation–condensation (Mechanism 3), which leads to neck growth without densification.[22] Additional mechanisms may be considered, however.

One alternative deformation mechanism is creep. While Coble creep via the grain boundaries is unlikely to contribute significantly for a powder where the crystal and particle sizes are similar, power law creep may. To test this, the equation for the densification rate of a powder compact by power law creep given by Helle et al. is used[21]:

$$\dot{\Delta} = 5.3(\Delta^2\Delta_0)^{1/3}\frac{x}{a}\left[\frac{\varepsilon_0}{\sigma_0^n}\right]\left(\frac{P}{3}\right)^n \tag{13}$$

where P is the densification driving force expressed as an applied hydrostatic pressure applied to the system, n is the power law creep exponent, and the terms in the square brackets, ε_0 and σ_0^n, are terms describing the power law creep behaviour. Other terms are as defined previously. In conjunction with this, the equation

linking the densification rate and the neck growth rate given by Wilkinson and Ashby[23] may be used:

$$\frac{\dot{\Delta}}{\Delta} = \frac{3}{2}\frac{\dot{x}}{a} \tag{14}$$

This gives, for the rate of neck growth by power law creep:

$$\dot{x}_{PL} = 3.53\frac{(\Delta^2\Delta_0)^{1/2}}{\Delta_0}x\left[\frac{\varepsilon_0}{\sigma_0^n}\right]\left(\frac{P}{3}\right)^n \tag{15}$$

An alternative expression for the quantity in the square bracket is given by Frost and Ashby by adapting the classical Dorn equation for power-law creep. This is designed to better describe power law creep over a wide range of temperatures and stresses,[20] incorporating both diffusion via the lattice and dislocation cores:

$$\frac{\varepsilon_0}{\sigma_0^n} = \frac{AD_{eff}Gb}{kTG^n} \tag{16}$$

where A is the Dorn constant, and b is the Burgers vector. Other terms are as defined previously, with the addition of D_{eff}, an effective diffusion coefficient formed by combining the coefficients of lattice and core diffusion (D_v and D_c):

$$D_{eff} = D_v\left[1 + \frac{10}{b^2}\left(\frac{\sigma_s}{G}\right)^2\frac{a_c D_c}{D_v}\right] \tag{17}$$

where a_c is the cross sectional area of a dislocation core. The effective pressure P driving the creep is that due to the surface tension of the solid alone, derived by Ashby as[19]:

$$P = \frac{3\gamma}{a}\Delta^2\left(\frac{2\Delta - \Delta_0}{1 - \Delta_0}\right). \tag{18}$$

Calculations of the rate predicted using Eq. (15) with Eqs. (16) and (18) over the range of conditions considered in Fig. 8 show that, within this range, power law creep never becomes the dominant mechanism. Mechanisms 3 and 4 of Swinkels and Ashby (Fig. 1) thus remain the two dominant time-dependent sintering mechanisms for single-crystalline NaCl powders in the temperature range considered here.

An additional mechanism that will have an effect is plastic yielding. As already discussed, research indicates that this mechanism may contribute significantly to the deformation occurring when pressure is applied at high temperatures, i.e. in hot pressing operations.[4] Ashby notes that densification by plastic yielding is quasi-instantaneous, and gives an equation for the density that will be reached for a particular applied pressure, P, before any other mechanism sets in[19]:

$$\Delta_{yield} = \left(\frac{(1 - \Delta_0)P}{1.3\sigma_y} + \Delta_0^3\right)^{1/3} \tag{19}$$

where terms are as defined previously, or as in Table 1, where their values are also given.

For the sintering case there is no externally applied pressure, and so we use Eq. (18) for the pressure between two particles due to the surface energy. As calculations show, plastic yielding
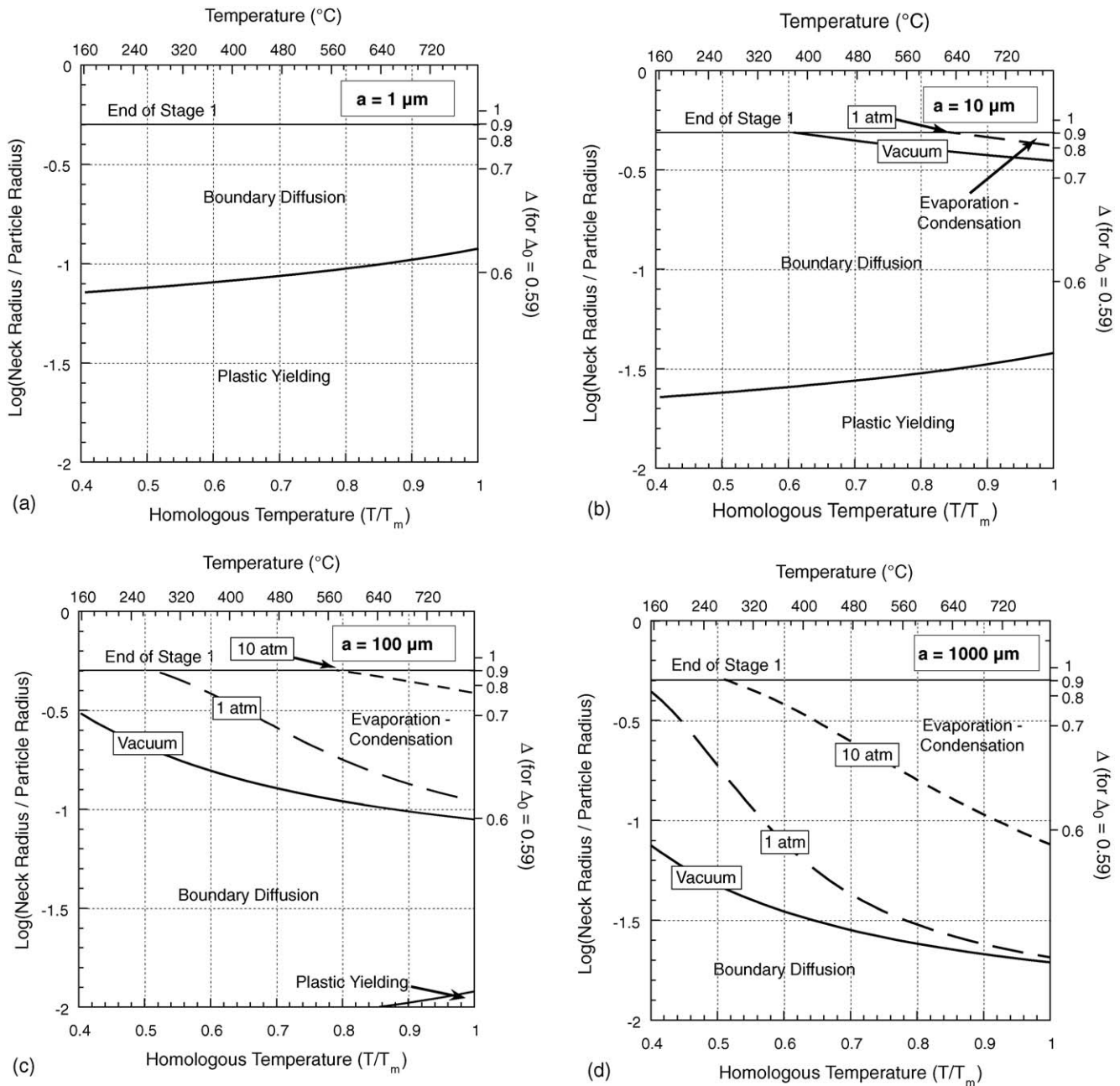
Fig. 8. Stage 1 sintering diagrams for sodium chloride, indicating the effect of changing the particle radius a ((a) 1 μm, (b) 10 μm, (c) 100 μm and (d) 1000 μm) on the position of the regions of dominance of the grain boundary diffusion, evaporation–condensation and plastic yielding mechanisms. For evaporation–condensation the equation has been considered for the conditions of vacuum, 1 atm inert gas pressure, and 10 atm inert gas pressure.

causes little densification without applied pressure; therefore, writing $\Delta \approx \Delta_0$ in the right-hand side of Eq. (18), Eq. (19) gives:

$$\Delta_{\text{yield}} \approx \left(\frac{2.31\gamma}{\sigma_y a} + 1 \right)^{1/3} \Delta_0 \qquad (20)$$

which can be used with the data in Table 1 to calculate the density reached by initial plastic yielding driven by surface tension alone.

The lines of transition in dominance between these three mechanisms with neck size and temperature are plotted in Fig. 8 for four different values of the initial particle radius, a. It is seen that plastic yielding indeed causes, with particles of a small diameter, at most a modest density increase (even for particles of 0.1 μm diameter, the initial plastic yielding density increase at room temperature is only to $\Delta = 0.63$ for a Δ_0 of 0.59). Where noticeable, plastic yielding is followed by grain boundary diffusion. The effect of plastic yielding is essentially nil with larger radius particles; in this case the condensation–evaporation mechanism dominates in the later stages, following initial densification by grain boundary diffusion.

4.3. Comparison of data with theory

The conclusion of Swinkels and Ashby that Mechanisms 3 and 4 are the only ones to dominate over long time scales thus agrees both with theory and the observation made here that, where densification is observed, the behaviour is consistent with the equations for grain boundary diffusion (see above, Section 4.1).

The boundary between the dominance of boundary diffusion (Mechanism 4) and evaporation–condensation (Mechanism 3) is shown in Fig. 2 for relative powder compact densities of 0.6, 0.61, 0.65, 0.7 and 0.9 (corresponding to x/a ratios of 0.09, 0.13, 0.22, 0.30 and 0.50, respectively), using, as before, an initial relative compact density, $\Delta_0 = \rho_i/\rho_o = 0.59$. The plastic yielding limit cannot be simply indicated as a region on Fig. 3, as the density attained by this mechanism varies with both particle size and temperature. It should therefore be remembered that, for submicron diameter particles, plastic yielding under Eq. (20) may specify the lowest density (or x/a ratio) line that will apply. For $a \geq 1\,\mu$m, on the other hand, this density is no larger than 0.6, leaving Fig. 2 unaffected.

Interestingly, the equations indicate that grain boundary diffusion will be initially dominant for all particle sizes and temperatures. This is because the evaporation–condensation mechanism contains a curvature difference term (Eq. (5)), whereas the boundary diffusion mechanism depends on a curvature difference squared (Eq. (6); although these two curvature differences correspond to different physical features, numerically they are very close until the neck is large). Past this initial stage, however, boundary diffusion-driven densification does not always remain dominant, particularly for the larger particle radii (see the lines for $\rho/\rho_o = 0.6$ or 0.61 in Fig. 2). Densification then stops because evaporation/condensation reduces significantly the neck curvature, in turn removing the driving force for grain boundary diffusion.

The small density changes that take place in these early stages of sintering could easily be missed experimentally, either because it is small compared to the experimental sensitivity, or because it might occur during heating up of the sample, before the initial measurement has been made. Thus, at the larger particle sizes, where the evaporation–condensation mechanism rapidly comes to dominate, no densification will be apparent. This was indeed the case in our own experiments on 400 μm diameter salt for all temperatures, and for the 150 μm diameter salt at 700 °C. At lower temperatures the latter salt showed densification; this is in agreement with the shape of isodensity mechanism transition lines in Fig. 2. One also notices that Stage 1 densification is predicted to reach completion (i.e., that boundary diffusion will remain dominant up to $\rho/\rho_o = 0.9$), at all temperatures provided the initial particle diameter is below 7.5 μm.

Overall, there is thus good agreement between theory and experiment, including the new data presented here. The exceptional result of Davidge, showing no densification even for a very fine powder below 400 °C, is best explained by the much reduced rate of any mechanism at this temperature. The equations indicate that the dominant mechanism will be grain boundary diffusion from boundary sources at 400 °C; however, the predicted rate of densification is so low that it should take roughly 3600 h for there to be a 0.1% increase in the density (a value probably close to the resolution in Davidge's experiments) for particles 1 μm in initial diameter. It is thus likely that the conclusion of Davidge was reached, not because there was no mechanism for densification, but rather because densification was too slow to be observed.

Examination of the experimental results in Fig. 2 shows that significant, measurable densification is only observed within reasonable timescales at temperatures above about $0.7T_m$. It is also clear from the plot that to obtain a fully sintered solid powder of the smallest diameter possible should be used, ideally less than 7.5 μm as, for this diameter and below, all temperatures of sintering will lead to the completion of Stage 1.

For the sintering of larger powders, as could be used in NaCl preforms for the production of metallic or ceramic foams by the replication method, once a certain density is reached densification will stop. For such applications this may not be a concern, as the aim is to leave space between the particles which may be infiltrated with material to produce the foam. The change to evaporation–condensation could in fact allow useful tailoring of the foam structure since this mechanism, while not driving densification, still influences the shape of the necks between the particles.

Where higher density is required using large particles (e.g. 400 μm NaCl particles with a goal of 0.8 relative density) another procedure, such as isostatic pressing (either hot or cold) would be required. Alternatively, control could be obtained using the ambient gas pressure during the sintering experiment, as we show in the next section.

4.4. Effect of gas pressure

We now relax the assumption that sintering is conducted in vacuum. We thus consider the influence of ambient inert gas on the kinetics of the evaporation–condensation mechanism.

Eq. (6) was implicitly derived under the assumption that the rate of atomic species condensation along the neck surface is rate limiting, the time for transport of solid phase atoms across the gas phase being negligible. With a finite-pressure sintering atmosphere (such as air), atom diffusion across the gas phase could become rate-limiting.

The transport path of atoms from the powder surface to the neck region at inter-particle contacts is complex; to simplify the problem, we recognize that the characteristic diffusion distance is the neck radius ρ. This is reasonable, as there is a much larger surface area of the particles that will be evaporating material to maintain the equilibrium partial vapour pressure, and the closest region to the neck will be found at a distance of ρ (see Fig. 1). Linking the concentration gradient to the pressure with the ideal gas law, $PV = NkT$, Fick's law writes:

$$J_{\text{Diffusion}} = D_g \left(\frac{P_v - P_\delta}{kT\rho} \right) \tag{21}$$

where D_g is the diffusion coefficient in the gas phase, P_δ is the partial vapour pressure of the solid phase molecules in the

gas along the neck surface and all other terms are as defined previously. Calculation of the mean free path using kinetic theory of gases shows that it is significantly less than ρ for all conditions where evaporation–condensation might dominate if the ambient pressure is larger than about 1000 Pa (0.01 atm). Under these conditions diffusion will not be in the Knudsen regime. D_g can then be estimated from the kinetic theory of gases[24]:

$$D_g = \frac{2}{3}\left(\frac{k^3}{\pi^3 m}\right)^{1/2}\frac{T^{3/2}}{Pd^2} \tag{22}$$

where d is the diameter of the diffusing species (assumed equal to the cube root of Ω), P is the pressure of the gas and other terms are as defined previously. Similar expressions for the diffusion of gas in a mixture and more accurate formulas (such as the Chapman–Enskog theory) exist, but the accuracy of Eq. (27) is sufficient for the present calculation since it provides a good estimate of D_g up to 10 atm pressure.[24]

As in the derivation of Eq. (6) by Kingery and Berg, the Langmuir formula gives the flux of material condensing at the neck[25]:

$$J_{Condensation} = C'(P_\delta - P_\rho) \tag{23}$$

where P_ρ is the partial vapour pressure in equilibrium with the neck with radius of curvature ρ. Parameter C' is given by:

$$C' = \frac{\alpha}{\sqrt{2\pi mkT}} \tag{24}$$

where α is a parameter describing the proportion of the condensing species that remain on the surface and are not re-evaporated ($0 < \alpha < 1$, here assumed to be 1); m is the atomic mass of the condensing species.

Combining Eqs. (21) and (23) to eliminate P_δ, one obtains:

$$J = C'\left[\frac{D_g(P_v - P_\rho)}{kT\rho C' + D_g}\right], \tag{25}$$

which, in the limits of $D_g \gg C'$ and $D_g \ll C'$ reduces to Eqs. (23) and (21), respectively.

As the rate of neck growth is equal to the flux multiplied by the atomic volume, we can write:

$$\dot{x} = \frac{\Omega C' D_g \Delta P}{kT\rho C' + D_g} \tag{26}$$

where $\Delta P = (P_v - P_\rho)$ is the difference in solid species partial pressure between a flat surface (neglecting the particle surface curvature compared to that of the neck); as in the derivation of Eq. (6) this is obtained from the Kelvin equation[5]:

$$\Delta P = \frac{\Omega\gamma P_v}{kT\rho} \tag{27}$$

with all terms as defined previously.

Eq. (26) thus represents the extension to an inert gas sintering atmosphere of the expression derived for vacuum by Kingery and Berg, Eq. (6).

As the ambient pressure increases, diffusion becomes increasingly rate-limiting (Eqs. (22) and (26)). This in turn will shift the lines dividing the dominance of the

evaporation–condensation from other mechanisms; these have been drawn on Fig. 8 for vacuum, for atmospheric pressure, and for an applied inert gas overpressure of 10 atm. As seen, pressure can have a significant effect on the evaporation–condensation mechanism, effectively eliminating it from the map for 10 μm radius particles, and significantly reducing the region of dominance for 100 and 1000 μm.

Since the evaporation–condensation mechanism does not result in densification while grain boundary diffusion does, the reduction of the rate of the former mechanism when sintering in inert gas will essentially preserve the driving force for densification by grain boundary diffusion. Using a finite-pressure inert sintering atmosphere such as open air will therefore enable an enhancement in the extent of densification that can be attained; this is particularly true when sintering at lower temperature, Fig. 8.

This conclusion is corroborated by experimental data in Fig. 2: if, indeed, Kingery and Berg's experiments were conducted in vacuum, densification was to stop at roughly 65% relative density according to theory, Fig. 2. In the present experiments, conducted in air under atmospheric pressure, more significant densification is predicted, Fig. 8; this was indeed observed, Fig. 2.

5. Concluding remarks

The behaviour predicted by the sintering diagram equations for NaCl at different conditions of particle size and temperature is shown to be consistent with experiment, including data in the literature and new data presented here. This leads to the conclusion that, after a small amount of densification by plastic yielding arising due to the surface energy forces, the initial sintering of NaCl powders is dominated by only two mechanisms across a wide range of particle sizes and temperatures, namely evaporation–condensation, yielding no densification, and grain boundary diffusion from grain boundary sources, yielding densification.

After very limited densification caused by plastic yielding, at the start of sintering grain boundary diffusion will always be the dominant sintering mechanism. Where the powder size is large, in practice above a value around 150 μm that decreases with decreasing temperature, densification stops in vacuum after only a small amount of dimensional change because the dominant mechanism for most of the sintering time is then evaporation–condensation. For smaller powders, typically around 100 μm and below, or when sintering under inert gas, grain boundary diffusion remains dominant for longer, enabling significant, if not complete, densification of powder preforms.

For conditions where densification is observed, fitting the data to known relationships and calculating the activation energy confirm that grain boundary diffusion drives the sintering process. Decreasing the sintering temperature increases the density at which densification ceases but also decreases the rate of sintering. A more interesting practical method to drive densification of NaCl may, rather, be to sinter in an atmosphere at finite pressure, such as open air.

Acknowledgements

References

1. San Marchi, C. and Mortensen, A., Infiltration and the replication process for producing metal sponges. In *Handbook of Cellular Materials*, ed. H. P. Degischer. Wiley-VCH, Weinheim, 2002. pp. 44–56.
2. Ashby, M. F., A first report on sintering diagrams. *Acta Metall.*, 1974, **22**(3), 275–289.
3. Swinkels, F. B. and Ashby, M. F., A second report on sintering diagrams. *Acta Metall.*, 1981, **29**, 259–281.
4. Ammar, A. A. and Budworth, D. W., Pressure sintering of NaCl and other ionic materials. *Trans. Br. Ceram. Soc.*, 1967, **3**, 93–105.
5. Kingery, W. D. and Berg, M., Study of the initial stages of sintering solids by viscous flow, evaporation–condensation and self-diffusion. *J. Appl. Phys.*, 1955, **26**(10), 1205–1212.
6. Moser, J. B. and Whitmore, D. H., Kinetics of sintering of sodium chloride in the presence of an inert gas. *J. Appl. Phys.*, 1960, **31**(3), 488–493.
7. Morgan, C. S., Hall, L. L. and Yust, C. S., Sintering of sodium chloride. *J. Am. Ceram. Soc.*, 1963, **46**(11), 559–560.
8. Ammar, A. A. and Budworth, D. W., Sintering of sodium chloride. *Proc. Br. Ceram. Soc.*, 1965, **3**(10), 185–193.
9. Ammar, A. A. and Budworth, D. W., Some comments on the sintering of sodium chloride and related materials. *Proc. Br. Ceram. Soc.*, 1969, **12**, 251–252.
10. Davidge, R. W., Densification of NaCl powder in air. *Proc. Br. Ceram. Soc.*, 1969, **12**, 245–249.
11. Lawless, W. N., Observations on pressure sintering of NaCl and other ionic materials. *J. Am. Ceram. Soc.*, 1968, **51**(4), 234–235.
12. Budworth, D. W., Comments on observations on pressure sintering of NaCl and other ionic materials. *J. Am. Ceram. Soc.*, 1968, **51**(12), 722.
13. Tomlinson, W. J. and Astle, G., Sintering kinetics of pure and $CdCl_2$-doped NaCl in air. *J. Mater. Sci. Lett.*, 1976, **11**, 2162–2165.
14. Sata, T. and Sakai, K., Sintering of NaCl powders. In *Proceedings of the 4th International Symposium on Science and Technology of Sintering*, ed. S. Shmiya, M. Shimada, M. Yoshimura and R. Watanabe. Elsevier Applied Science, London, 1987, pp. 249–254.
15. Sata, T., Expansion during sintering of NaCl powders. *Ceram. Int.*, 1994, **20**, 39–47.
16. Thompson, R. J. and Munir, Z. A., Influence of particle size on the sintering kinetics of ultrapure sodium chloride. *J. Am. Ceram. Soc.*, 1982, **65**(6), 312–316.
17. Taylor, N., Dunand, D. C. and Mortensen, A., Initial stage hot pressing of monosized Ti and 90%Ti–10%TiC powders. *Acta Metall. Mater.*, 1993, **41**, 955–965.
18. Goodall, R., Marmottant, A., Despois, J.-F., Salvo, L. and Mortensen, A., Replicated microcellular aluminium with spherical pores. In *Proceedings of Metfoam 2005*, ed. H. Nakajima. Japan Institute of Metals, 2005.
19. Ashby, M. F., In *Powder Metallurgy: An Overview*, ed. I. Jenkins and J. V. Wood. The Institute of Metals, London, 1991, pp. 144–166.
20. Frost, H. J. and Ashby, M. F., *Deformation Mechanism Maps – The Plasticity and Creep of Metals and Ceramics*. Pergamon, Oxford, 1982.
21. Helle, A. S., Easterling, K. E. and Ashby, M. F., Hot-isostatic processing diagrams—new developments. *Acta Metall.*, 1985, **33**(12), 2163–2174.
22. Kingery, W. D., Bowen, H. K. and Uhlmann, D. R., *Introduction to Ceramics* (*2nd ed.*). J. Wiley & Sons, New York, 1976, pp. 469–490.
23. Wilkinson, D. S. and Ashby, M. F., Pressure sintering by power law creep. *Acta Metall.*, 1975, **23**, 1277–1285.
24. Poirier, D. R. and Geiger, G. H., *Transport Phenomena in Materials Processing*. TMS, Pennsylvania, 1994.
25. Langmuir, I., The vapour pressure of metallic tungsten. *Phys. Rev.*, 1913, **2**(5), 329–342.
26. San Marchi, C. and Mortensen, A., Deformation of open-cell aluminium foam. *Acta Mater.*, 2001, **49**, 3959–3969.
27. Ashby, M. F., *Operating Manual for HIP 6.0: Software for Constructing Maps for Sintering and Hot Isostatic Pressing*. Cambridge University Engineering Department, Trumpington St, Cambridge, UK, 1990.
28. Lide, D. R., *CRC Handbook of Chemistry and Physics* (*82nd ed.*). CRC Press, New York, 2001.